

Holographic detection for fast fringe projection profilometry of deep micro-scale objects

CONOR RYAN, 1,2,* TOBIAS HAIST, AND STEPHAN REICHELT 1

Abstract: Phase-shifting Fringe projection profilometry (FPP) excels in 3D measurements for many macro-scale applications, but as features-of-interest shrink to the microscopic scale, depth-of-field limitations slow measurements and necessitate mechanical adjustments. To address this, we introduce digital holography (DH) for fringe image capture, enabling numerical refocusing of defocused object regions. Our experiments validate this approach and compare depth measurement noise with other DH and FPP methods. Results show that for slight defocus, incoherent FPP surpasses coherent techniques, while under significant defocus, the new method minimizes measurement uncertainty and matches the performance of other DH techniques, facilitating faster measurement of deep, micro-scale objects.

Published by Optica Publishing Group under the terms of the Creative Commons Attribution 4.0 License. Further distribution of this work must maintain attribution to the author(s) and the published article's title, journal citation, and DOI.

1. Introduction

Phase-Shifting Fringe Projection Profilometry (PS-FPP) is a non-contact, non-destructive, optical 3D shape measurement technique. In PS-FPP, triangulation is performed with a camera and an off-axis projector. A phase-shifted sinusoidal pattern is projected onto the object surface, whose image from a different perspective is modulated by object height. The phase of the pattern is calculated over the image, unwrapped and transformed from image-space to object-space before evaluating the topography of the object. Each step in the process has many variants, presented in an overview by [1].

Projection systems using incoherent light sources enable moderate measurement volumes to be measured with very low measurement uncertainty. Due to speckles, coherent light sources typically exhibit much larger uncertainty [2], but can be extremely compact [3–5]. Also, fringes produced by coherent interference of plane waves are never defocused.

In macroscopic applications, large 3D scenes can be measured with PS-FPP using a few detector captures, and hence it has enjoyed widespread success. Meanwhile, FPP configurations for microscopy, reviewed by [6], have more barriers to application. One issue is that high accuracy measurements are possible only within a small field-of-view and depth-of-field. For example, a microscope with object-sided numerical aperture (NA) of 0.3, magnification (M) of 1 and 5 µm pixels, has geometrically-limited depth-of-field of about 17 µm. Field curvature and deviation from plane of calibration further limit depth range. Extended measurement depth is usually achieved with mechanical [7] or electro-optical scanning [8], increasing measurement times for deep microscopic objects. Defocus can occur in projection and detection. Defocus applies a low-pass filter to spatial frequencies and reduces the modulation of sinusoidal fringes. Depth from object defocus [9], fringe projection defocus [10] and defocused binary pattern projection [11] utilizes these defocus effects but are still range limited without mechanical scanning.

The measurement range of microscopic PS-FPP may be extended using digital holography. Digital Holography (DH) measures the entire complex field of light from an object in a single or few captured interferograms. The phase and amplitude of the field can be calculated at any plane

https://doi.org/10.1364/OE.549266 © 2025 Received 18 Nov 2024; revised 10 Dec 2024; accepted 11 Dec 2024; published 7 Jan 2025

¹Institute for Applied Optics (ITO), University of Stuttgart, 70569 Stuttgart, Germany

²Institute of Optical Sensor Systems, German Aerospace Center, 12489 Berlin, Germany

^{*}conor.ryan@dlr.de

in object space, which is termed 'numerical refocusing'. By using interference-based fringe projection and capturing the PS-FPP scene with DH instead of a camera, defocus of the camera and projection may be eliminated and deep objects may be measured with a single capture per fringe pattern projected.

Ptytulak et al. have already proposed a combination of DH and Fourier Transform FPP as a 3D shape and deformation measurement method [12]. Yet their approach was to a different end, and DH was used to measure smooth objects/deformations with slow height variation within a few-microns range, while FPP measured large object variations. Thus their DH application was limited to shallower objects than their FPP.

In contrast, we introduce DH to extend the measurement volume of FPP, naming the technique DH-supported FPP (DH-FPP). We derive an expected relationship between depth-noise and defocus of imaging and projection for incoherent-, coherent- and DH-FPP. With this relationship we show that an exponential rise in depth uncertainty, caused by defocus, can be avoided whilst still using FPP algorithms. We explain similarities and differences of DH-FPP approach to another holographic approach, DH-AOI [13]. We underscore the complexities in the individual and combined techniques. To enable comparison, we suggest a setup capable of measuring depth uncertainty with all 4 techniques on standard step objects under equal conditions. We discuss expectations, measurements, similarities between techniques and limitations.

2. Theory

Capturing a sinusoidal projection on a flat surface with focused imaging and projection produces an intensity distribution at the detector $I_{\text{det}}(x) = A + B\cos(2\pi x/T)$, where A is a background intensity level, B is intensity modulation and T the fringe period. Height uncertainty for incoherent FPP can been modeled from projection to 3D geometry as a sequence of uncertainty transfer models [14]. When temporal phase shifting algorithms (s. Eq. (6)) are applied, normally distributed intensity noise σ_I can be mapped to phase noise σ_φ by [15]:

$$\sigma_{\varphi} = \frac{\sqrt{2}}{\sqrt{N}B}\sigma_{I} \tag{1}$$

Where N is the number of phase-shifted captures. Assuming a linear relation between unwrapped phase and object height, the standard deviation of the measured object height σ_z is proportional to 1/B.

One effect of defocus is to imparting radiometric losses. As the object surface moves further from the entrance aperture, the captured solid angle of light reduces with $(z+\delta)^2/z^2$, where z is the distance to the plane of focus.

At large levels of defocus, geometric effects dominate the PSF [16]. A Gaussian PSF, though not predicted by geometric optics, is commonly used as a simplification and is seen experimentally [9,17]. Modelling the defocused projection and imaging as sequential convolutions of Gaussian kernels with $I_{\text{display}}(x) = A + B\cos(kx)$ yields:

$$I'_{\text{det}}(x) = A + B \exp\left[\frac{-k^2(\sigma_p^2 + \sigma_o^2)}{2}\right] \cos(kx)$$
 (2)

Where σ_o , σ_p are standard deviations of the Gaussian PSFs of observation and projection. They define the gaussian PSF FWHM diameter $d = 2\sqrt{2 \ln(2)}\sigma$, which is proportional to defocus δ and NA for small aperture angles as well, inferring $\sigma^2 \propto \delta^2 \text{NA}^2$. This model assumes unitary magnification, local object flatness and homogenous reflectivity. Considering radiometric losses

and comparing modulation before and after defocus yields (derivation in Supplement 1):

$$\frac{B'}{B} = \left(\frac{z}{z+\delta}\right)^4 \exp\left[2K(\delta_o^2 N A_o^2 + \delta_p^2 N A_p^2)/\pi^2 T^2\right]$$
(3)

where *B*' is the fringe modulation after defocus and *K* a constant of proportionality. We infer that the standard deviation of measured object height for incoherent FPP will scale with this ratio.

The projected fringe pattern for coherent and DH is produced by two-beam interference and suffers no defocus. Defocus of observation is present for coherent FPP, while it is removable for DH-FPP and DH-AOI. However, the required dynamic range for holography is higher due to the added reference beam. Coherent illumination also brings coherent noise. FPP simulations suggested empirically that coherence effects impact phase noise with the relation [18]:

$$\sigma_{\varphi} = R \left(a_1 C + \frac{a_2}{B} \right) \tag{4}$$

where a_1 and a_2 are constants, C is the speckle contrast and R is additive white noise at detector and projector. The first term suggests that speckle noise is fundamentally limiting, while the second term suggests that modulation reductions further increase noise. The fundamental speckle limit for triangulation-based methods has been shown to be [19]:

$$\sigma_z = \frac{\lambda C}{2\pi N A \sin \beta} \tag{5}$$

where λ is the wavelength of light, NA the numerical aperture of observation and β the triangulation angle. An explanation for the second term is speckle phase decorrelation noise, which occurs when speckled intensity captures are compared and increases with defocus, surface roughness and tilt [20]. References [21,22] show analytically that it is inversely proportional to modulation, while [23] shows speckles must be highly resolved or highly unresolved to reduce decorrelation noise in coherent FPP. As defocus can be set to near zero numerically, we expect DH-FPP to have near-constant depth uncertainty over a large defocus range with some variation due to radiometric losses.

Two alternate setups are plausible, using very small or very large pixels. For holographic applications however, reducing pixel size allows a laterally larger measurement volume [24] and is the approach taken here. Each resolved speckle has different modulation, such that setting a modulation threshold removes whole speckles and improves measurement noise [25].

The integration of DH into an FPP technique, not merely as adjacent technique but also as a preprocessing step in the FPP data evaluation chain is complex, as the sources of noise in depth-measurement by FPP and DH are numerous. Combining the techniques mixes the sources of depth-noise and has them become inputs to each other. Choices in setup and algorithm variants become challenging, so the paper contributes not only a comparison of experimental depth-uncertainty of the new and old techniques, but also an investigation into the best approaches. As a simple example, reducing the wavelength changes triangulation noise, decorrelation and interferometrically generated fringe period. The measurement setup and DH approaches used are the result of a review of the literature, early experimentation and trade-offs under the realistic constraints of working distance and setup size.

3. Methods and materials

The setup for measurements of both incoherent PS-FPP and DH-PS-FPP is shown in Fig. 1. The optical axes of detection and projection differ by the triangulation angle β . Incoherent and interferometric projection coincide. The detector arm contains a ZWO ASI 183 camera with a Sony IMX183CLK-J image sensor (2.4 μ m pixel pitch), a 50 mm focal length lens, imaging

with a magnification of 1.9, and a polarizer for enhancing interference visibility. The incoherent projection system consists of a front-illuminated LCOS (LED Pico projector from AAXA Tech. Inc., projection optics removed) and a microscope formed by lenses L2 and L3, which projects the LCOS on the object with a magnification of 1.2. The LCOS displays 1D phase-shifted sinusoidal patterns with fringes running out-of-plane.

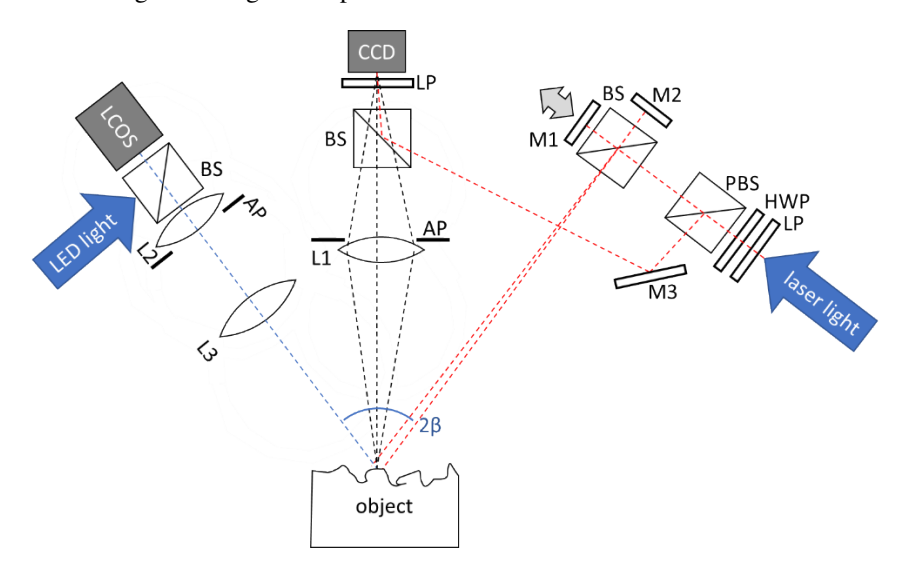


Fig. 1. Symmetric setup used for comparative deep-microscopic-object measurements of PS-FPP with incoherent illumination and DH-PS-FPP with coherent illumination. M1, M2, M3 are mirrors, L1, L2, L3 are lenses, (P)BS are (polarization-) beam splitters, AP are limiting apertures, HWP a half-wave plate and LP, a linear polarizer to enhance interference visibility.

The interferometric projection uses a Michelson interferometer with one slightly tilted mirror to generate fringes in object space. One mirror is piezo-actuated on-axis for phase shifting. To create off-axis holograms at the detector, a reference beam is sampled prior to the interferometric projector then recombined with light from the object. A half-wave plate balances beam powers at the detector. Blocking the reference beam allows for imaging of the coherent fringe pattern. Recording holograms whilst sequentially blocking light from M1 and M2 allows DH-AOI. The aperture in the incoherent projection microscope limits the highest spatial frequencies to control depth-of-field. The camera's object-side NA was reduced to 0.05 to resolve speckles and optimize spatial bandwidth for off-axis DH.

For DH-FPP, N numerically refocused holograms are generated by filtering out DC and twin image components of the raw hologram from its Fourier transform, then propagating until focus via the angular spectrum method. This generates a set of N phase-shifted pattern images for FPP processing. For N phase shifts evenly distributed around 2π , the phase map $\Phi(x,y)$ for FPP was calculated as [26]:

$$\Phi(x,y) = \tan^{-1} \left(\frac{\sum_{n=0}^{N-1} I_n(x,y) \sin(2\pi n/N)}{\sum_{n=0}^{N-1} I_n(x,y) \cos(2\pi n/N)} \right)$$
(6)

where I_n is the intensity in the n^{th} hologram or image, and (x,y) are the lateral coordinates in object space. The intensity modulation B(x,y) can be calculated as:

$$B(x,y) = \frac{2}{N} \sqrt{\left[\sum_{n=0}^{N-1} I_n(x,y) \sin\left(\frac{2\pi n}{N}\right) \right]^2 + \left[\sum_{n=0}^{N-1} I_n(x,y) \cos\left(\frac{2\pi n}{N}\right) \right]^2}$$
(7)

Equations (6) and (7) are valid for both coherent and incoherent fringe projection approaches. For DH-AOI, the illumination from M1 and M2 are separately, holographically recorded. The argument of the refocused holograms is the speckled object phase and the difference between two different speckled object phase distributions yields a phase map $\Phi(x,y)$.

The unambiguous measurement range of DH-AOI, DH-FPP and coherent FPP are in principle identical and approximated by $\mathcal{N}\Delta\theta\sin\beta$, where $\Delta\theta$ is the difference in angle of incidence of illumination. For the same object, DH-FPP and DH-AOI use different measurement setups and algorithms, yet arrive at the same mathematical result. Both are subject to coherent and phase-decorrelation noise, yet different algorithmic and detector noise contributions. Both may have comparative noise reductions for different reasons: DH-FPP entails more measurements, while DH-AOI can use longer integration times per capture. The phase-to-height transformation is applied to obtain the object height:

$$h\left(\frac{x}{M_o}, \frac{y}{M_o}\right) = \frac{T(M_p, M_o) \left(\Phi\left(\frac{x}{M_o}, \frac{y}{M_o}\right) + m2\pi\right)}{2\pi \sin\beta} \tag{8}$$

where T is the fringe period in the plane of the object, M_o , M_p are observation and projection magnification and m is the fringe order. Due to phase-shifting inaccuracy of the piezo transducer used, the number of captures N was increased to 11 for coherent- and DH-FPP to suppress a double-frequency phase error [27]. Phase shifting algorithms for arbitrary, unknown phase steps (e.g. [28]) were experimentally found unable to handle the speckled reference field.

Flat which represent the most cooperative shape. One effect of (locally) increasing surface slope for certain rough surfaces is the change of scattered light incident in the entrance pupil of the (holographic) camera, resulting in a change of the signal-to-noise ratio of the captured fringes. Of course, this effect also depends strongly on the surface roughness and observation NA. Projected fringe spacing is also increased locally, changing the period/speckles and period/pixels ratios. The period of holographic micro-fringes also changes, as sloped surface and reference beam wavefronts differ. Algorithms for phase retrieval and unwrapping may be adapted for specific surface shapes but in general will be noticeably influenced. Phase decorrelation is also sensitive to surface slope. A theoretical and experimental comparison of the complex effects of local surface slope in all four techniques is complicated and requires further investigation.

4. Results

Measurements of milled aluminum step profiles coated with white dental scan spray (ScanTist 3D Permenant) were performed with equal period, camera NA and triangulation angle β in each case. The samples were then measured with an incoherent PS-FPP instrument (Keyence VR-5200) to confirm roughness (Ra $\sim 3~\mu m)$ and step height were unaffected by coating. The top surface of the step profile was always in-focus and the bottom surface further away from the camera. Figure 2 shows exemplary captured images for incoherent and coherent FPP and merged-focus DH-FPP images. The magnification varies for refocused DH images with changing object and image distances, but was calculatable with knowledge of the setup and numerical refocusing distances. The fringe modulation at 5 mm defocus is invisible to human eyes without holographic refocusing. The intensity profile of the reconstructed holographic measurements is limited by the diameter of the reference beam. This is a limitation to our DH-FPP setup specifically, not the technique generally.

Phase was calculated in rectangular regions for the focused and defocused surfaces. Phase standard deviation was calculated then for each pixel column. The minimum standard deviation for defocused surfaces is plotted below in Fig. 3.

Coherent noise dominates depth measurement noise for all coherent techniques at low defocus, setting a baseline noise which is reducible by thresholding or further increasing *N*. Increasing

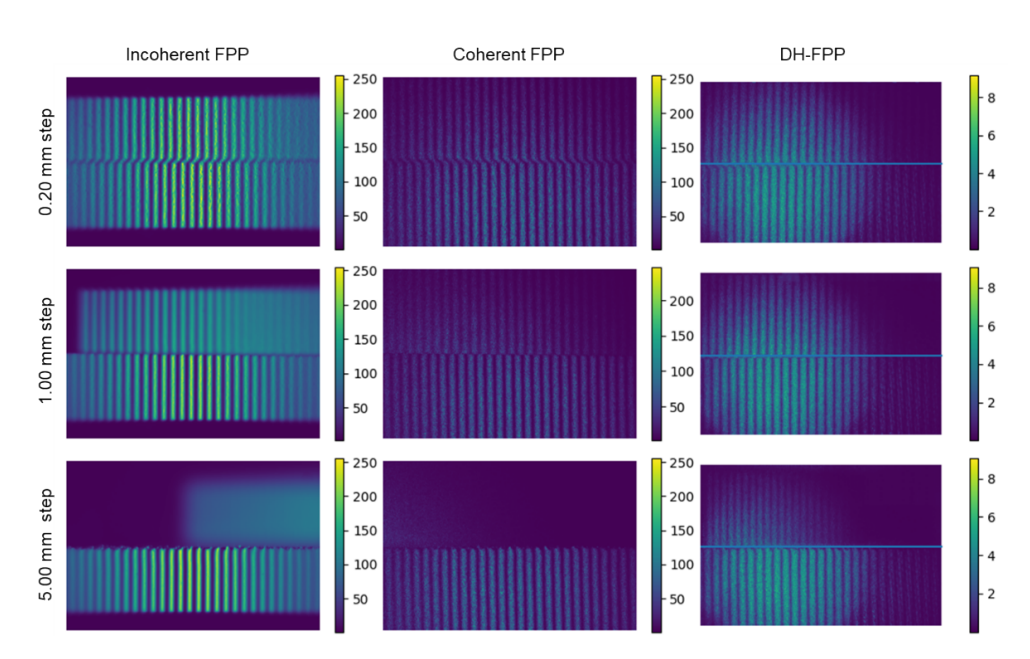


Fig. 2. Unprocessed captured frames from Incoherent FPP, Coherent FPP compared to DH-FPP merged-focus, processed DH-FPP frames which are refocused above the blue line.

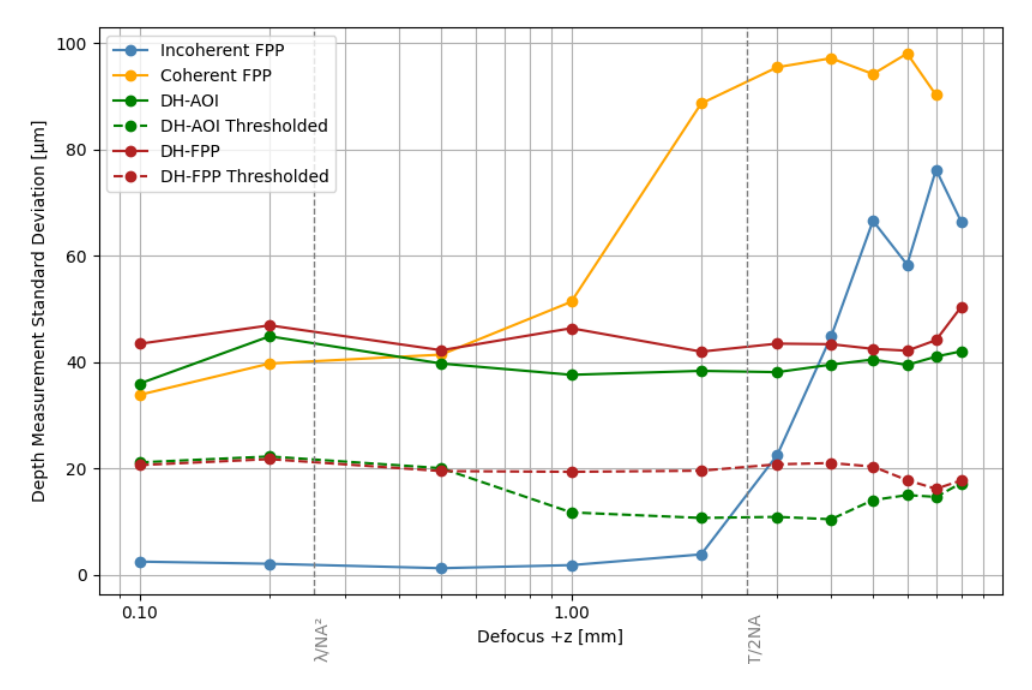


Fig. 3. Standard deviation of depth measurement at varying levels of defocus (plotted in logarithmic scale) with identical imaging NA for the following techniques: Coherent Fringe Projection Profilometry (FPP), Incoherent FPP, Digital Holography supported FPP (DH-FPP), modulation-thresholded DH-FPP and multiple angle-of-incidence digital holography (DH-AOI). For context, grey dashed lines indicate defocus set at the depth-of-field of observation and the defocus at which the spot diameter is equal the fringe period.

defocus impacts coherent FPP earliest, as defocus increases phase decorrelation and speckle contributors to each pixel. Exponential growth in measurement noise with defocus for incoherent FPP gives an advantage to DH-FPP where the defocus is very large. Applying a global 50% modulation threshold within the ROI to DH techniques accentuates the advantage. Applying holography to refocus for fringe projection is applying two sets of phase computation algorithms. Yet the differences between coherent FPP, DH-FPP and DH-AOI, due to setup and algorithmic noise, are much smaller than the in-focus coherent noise level. Despite different approaches to calculating object height, DH-FPP and DH-AOI have similar uncertainty across the defocus range. DH-AOI has a simpler setup and fewer needed captures, so it should be preferred over FPP techniques for fast topographic measurement of strongly defocused microscopic objects.

The effects of numerical aperture on defocus-induced depth uncertainty increases are plotted for these techniques in Fig. 4. Tolerance to defocus is reduced in coherent and incoherent FPP with increasing NA, while the depth-uncertainty of DH is unaffected. The 16 mm pupil measurement was not possible for DH due to the constraint to resolve speckles and interferometric micro-fringes at the detector for off-axis holography. In other words, a 16 mm pupil would cause overlap of the +1, 0 and -1 orders in the spatial frequency domain, adding significantly to measurement noise. This is a limitation of the detector used in this setup. If the DH techniques were operating at the fundamental speckle limit, the noise level (\sim 40 μ m) should have varied with NA. Therefore, we can assume the DH methods were not operating at the fundamental speckle limit and could be further improved.

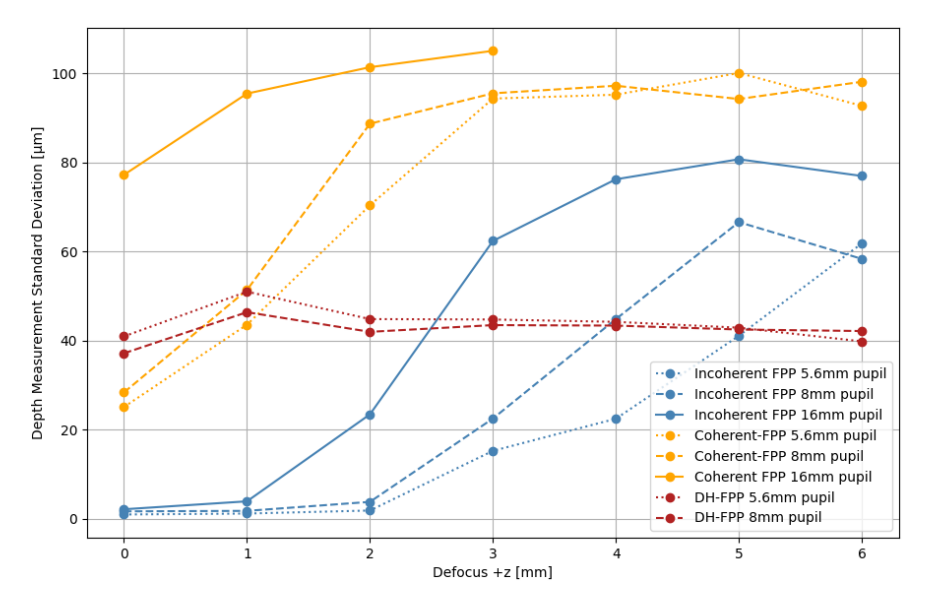


Fig. 4. Effect of camera pupil diameter on depth uncertainty measurements. Increasing line density corresponds to increasing numerical aperture.

The quality of fringes is of major importance for achieving low height uncertainty in combination with good lateral resolution. Indeed, the coherent techniques have here a disadvantage due to interference effects (speckles) compared to incoherent methods. On the other hand, the coherent techniques help to achieve a better quality if defocus or depth of focus are a practical issue (see Fig. 3). To improve the results of coherent approaches, one might use temporal averaging techniques (e.g. rotation of a diffuser) or a change of other system parameters, most notably the triangulation angle. At the cost of lateral resolution, algorithms that use some kind of spatial averaging would further improve the height accuracy.

Figure 5 shows refocused DH-FPP measurements of a complex object (coin) with sloped specular surfaces, placed 2 mm from the plane of best focus. The slope angles and orientation determine which specular reflections improve or destroy fringe modulation. The modulation-based thresholding applied to the image results in missing data points in the height map.

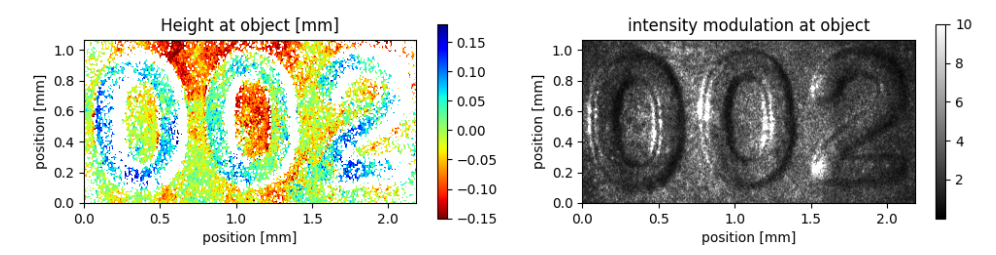


Fig. 5. Height map and corresponding intensity modulation from refocused DH-FPP measurements of an embossed coin surface placed 2 mm from the plane of best focus

5. Conclusion

DH-FPP was introduced to alleviate the depth-of-focus issue for microscopic FPP. Measurement depth uncertainty at different levels of defocus was compared with that of incoherent and coherent FPP as well as DH-AOI. The results show lower measurement noise for large levels of defocus when numerical refocusing of fringes and modulation thresholding are exploited. This allows measurement of highly detailed, deep objects without the need to translate and repeat measurements at different planes of focus. However, DH-AOI was found to have similar uncertainty while potentially being simpler and faster than DH-FPP. These results should help engineers dealing with topography measurement of variable, unknown object sizes to implement the fastest and most precise methods.

Acknowledgments. The authors would like to thank the student Alina Malow for assistance in with measurements.

Disclosures. The authors declare no conflicts of interest.

Data availability. Data underlying the results presented in this paper are not publicly available at this time but may be obtained from the authors upon reasonable request.

Supplemental document. See Supplement 1 for supporting content.

References

- S. S. Gorthi and P. Rastogi, "Fringe Projection Techniques. Whither we are?" Opt. Lasers Eng. 48(2), 133–140 (2010).
- 2. G. Häusler and S. Ettl, "Limitations of Optical 3D Sensors," in *Optical Measurement of Surface Topography*, R. Leach, ed. (Springer, 2011, Chap. 3).
- 3. K.-I. Joo, M. Kim, M.-K. Park, et al., "A 3D Optical Surface Profilometer Using a Dual-Frequency Liquid Crystal-Based Dynamic Fringe Pattern Generator," Sensors 16 (2016).
- 4. T. Huang, X. Li, X. Fu, et al., "Integrating-bucket phase stabilization method for fiber-optic fringe projector," Opt. Laser Technol. 118, 192–197 (2019).
- P. Shanmugam and K. Falaggis, "Fringe projector with submillimeter fringe spacing at a meter-scale field of view," Appl. Opt. 62(31), 8334–8341 (2023).
- Y. Hu, Q. Chen, S. Feng, et al., "Microscopic fringe projection profilometry: A review," Opt. Lasers Eng. 135, 106192 (2020).
- K. Körner, R. Windecker, M. Fleischer, et al., "One-grating projection for absolute 3D profiling," Opt. Eng. 40(8), 1653 (2001).
- X. Hu, G. Wang, Y. Zhang, et al., "Large depth-of-field 3D shape measurement using an electrically tunable lens," Opt. Express 27(21), 29697–29709 (2019).
- A. P. Pentland, "A New Sense for Depth of Field," IEEE Trans. Pattern Anal. Mach. Intell. PAMI-9(4), 523–531 (1987).
- Y. Zheng, Y. Wang, and B. Li, "Active shape from projection defocus profilometry," Opt. Lasers Eng. 134, 106277 (2020).

- S. Lei and S. Zhang, "Flexible 3-D shape measurement using projector defocusing," Opt. Lett 34(20), 3080–3082 (2009).
- M. Prytulak and R. Jozwicki, "Application of digital holography to surface shape measurement using an interferometric fringe projection system," in *Optical Measurement Systems for Industrial Inspection III*, Vol. 5144 of Proc. of SPIE (SPIE, 2003).
- 13. I. Yamaguchi, S. Ohta, and J. Kato, "Surface contouring by phase-shifting digital holography," Opt. Las. Eng **36**(5), 417–428 (2001).
- 14. S. Lv and Q. Kemao, "Modeling the measurement precision of Fringe Projection Profilometry," Light:Sci. Appl. 12(1), 257 (2023).
- J. Li, L. G. Hassebrook, and C. Guan, "Optimized two-frequency phase-measuring profilometry light-sensor temporal-noise sensitivity," J. Opt. Soc. Am. A 20(1), 106–115 (2003).
- 16. J. W. Goodman, Introduction to Fourier Optics (McGraw Hill, 1968).
- 17. P. Favaro and S. Soatto, "A geometric approach to shape from defocus," IEEE Trans. Pattern Anal. Mach. Intell. **27**(3), 406–417 (2005).
- L. Kinell and M. Sjödahl, "Robustness of reduced temporal phase unwrapping in the measurement of shape," Appl. Opt. 40(14), 2297 (2001).
- R. G. Dorsch, G. Häusler, and J. M. Herrmann, "Laser Triangulation: fundamental uncertainty in distance measurement," Appl. Opt. 33(7), 1306 (1994).
- A. E. Ennos, "Speckle Interferometry," in Laser Speckle and Related Phenomena, J. C. Dainty, ed. (Springer, 1975, Chap. 6).
- M. Lehmann, "Decorrelation-induced phase errors in phase-shifting speckle interferometry," Appl. Opt. 36(16), 3657 (1997).
- S. Rosendahl, E. Hällstig, P. Gren, et al., "Phase errors due to speckles in laser fringe projection," Appl. Opt. 49(11), 2047 (2010).
- H. Liu, G. Lu, and S. Wu, "Speckle-induced phase error in laser-based phase-shifting projected fringe profilometry,"
 J. Opt. Soc. Am. A 16(6), 1484 (1999).
- U. Schnars and W. Jüptner, "Direct recording of holograms by a CCD target and numerical reconstruction," Appl. Opt. 33(2), 179 (1994).
- 25. M. Lehmann, "Measurement optimization in speckle interferometry: the influence of the imaging lens aperture," Opt. Eng. 36(4), 1162 (1997).
- J. H. Bruning, D. R. Herriot, D. P. Gallagher, et al., "Digital Wavefront Measuring Interferometer for Testing Optical Surfaces and Lenses," Appl. Opt. 13(11), 2693 (1974).
- J. Schwider, R. Burow, K.-E. Elssner, et al., "Digital wave-front measuring interferometry: some systematic errors," Appl. Opt. 22(21), 3421 (1983).
- L. Z. Cai, Q. Liu, and X. L. Yang, "Phase-shift extraction and wave-front reconstruction in phase-shifting interferometry with arbitrary phase steps," Opt. Lett 28(19), 1808 (2003).